Journal of The Electrochemical Society, **161** (9) A1200-A1212 (2014)
0013-4651/2014/161(9)/A1200/13/$31.00 © The Electrochemical Society

Analysis and Three-Dimensional Modeling of Vanadium Flow Batteries

Yun Wang[*,z] **and Sung Chan Cho**

Renewable Energy Resources Laboratory (RERL), Department of Mechanical and Aerospace Engineering, The University of California, Irvine, California 92697-3975, USA

This study presents 1.) a multi-dimensional model of vanadium Redox Flow Batteries (RFB); 2.) rigorous explanation of pore-level transport resistance, dilute solution assumption, and pumping power; and 3.) analysis of time constants of heat and mass transfer and dimensionless parameter. The model, describing the dynamic system of a RFB, consists of a set of partial differential equations of mass, momentum, species, charges, and energy conservation, in conjunction with the electrode's electrochemical reaction kinetics. The governing equations are successfully implemented into three-dimensional numerical simulation of charging, idling, and discharging operations. The model, validated against experimental data, predicts fluid flow, concentration increase/decrease, temperature contours and local reaction rate. The prediction indicates a large variation in local reaction rate across electrodes and the time constants for reactant variation and temperature evolution, which are consistent with theoretical analysis.

Manuscript submitted March 13, 2014; revised manuscript received May 16, 2014. Published May 21, 2014.

Flow batteries, capable of storing large quantity of energy, have great potential to increase power flexibility and improve dynamic response to energy demand.[1–3] Flow batteries are a rechargeable electrochemical energy system, in which electrolytes contain one or more dissolved electroactive species, and the chemical energy in electrolytes is reversibly converted to electricity. The electrolyte is stored externally in a tank, and delivered to the reactor. Batteries can be recharged by replacing electrolytes, similar to conventional vehicles, or by external electric power that is similar to secondary batteries. Flow battery technology offers advantages in energy storage and conversion, including: 1.) large capacity (determined by the external tank volume); 2.) negligible degradation when left completely discharged for long periods; 3.) charge/recharge through electrolyte replacement or external power source; and 4.) no permanent damage when electrolytes are accidentally mixed. Among the major types of flow batteries, the vanadium redox flow battery is a type of rechargeable flow battery that employs vanadium ions at different oxidation states to store chemical potential energy.

Since the concept of redox flow battery (RFB) was first introduced by Posner at 1955,[4] various RFB systems have been developed. NASA investigated the Iron/titanium (Fe/Ti) RFB in its early flow battery program, and the RFB exhibit significant crossover and performance decay.[5] The iron/chromium (Fe/Cr) system was investigated by NASA in 1970s partly due to its low cost. The system had severe cross-over and increasing membrane resistance,[6,7] and required catalyst for chromium redox couple.[8] The bromine/polysulphide RFB is another type that has been extensively studied,[9] sodium bromide and sodium polysulfide are used as electrolyte, which are widely available and low in price. However, cross-over through separators causes formation of Br_2 and precipitation of sulfur. Vanadium RFBs are a type of flow battery that employs two oxidation states of the same element as anolyte and catholyte, respectively. Carbon felts and sulphuric acid are the popular electrode and electrolyte materials, respectively. A historical overview of materials research and development for vanadium RFBs was recently provided by Parasuraman et al.[10] Walsh and coworkers reviewed their challenges and applications,[11] and commercialization and cost.[12] Early study showed the surface treatment of the glassy carbon electrode greatly affects the electrochemical activity of the V(III)/V(II) couple in H_2SO_4.[13] Rychcik and Skyllas-Kazacos[14] employed the vanadyl sulfate solution in sulphuric acid as electrolyte and an ion-selective membrane as separator to construct a RFB. Their experimental results indicated the battery's energy/power density of 5 kW h/1 kW, which is similar to lead/acid and nickel/cadmium batteries. Skyllas-Kazacos et al. reported an energy efficiency of up to 90% and for a 1 kW prototype RFB system that used 1.5–2 M vanadium sulfate in sulphuric acid.[15] The system achieved over 85% of theoretical capacity in the discharge current range of 30–120 A. Currently, vanadium RFBs have been commercialized in stationary energy storage system and large-scale load-leveling systems for renewable energy sources such as wind turbine in Australia, Thailand, and Japan. It also showed potential as emergency back-up with over 80% energy efficiency.[16] For stationary and grid applications, energy density is not a critical factor; and the RFB's power can be readily scaled to Mega Watt and energy capacity to the MW h level.

Modeling vanadium RFBs have been attempted by several groups. Al-Fetlawi et al. developed a non-isothermal two-dimensional (2-D) model by taking into account the waste heat generation of RFBs.[17] They showed that an effective cooling strategy is required for RFBs in high-temperature environments and under high loads to avoid large temperature increases. Shah et al.[18] proposed a control-oriented model for RFBs, which accounts for the major voltage loss mechanisms and electrolyte circulation, and relates the RFB performance to key system properties. You et al. developed a 2-D stationary model to investigate a few parameters in RFBs including current density, electrode porosity and local mass transfer coefficient.[19] Their approach was based on the 2-D transient model of Shah et al.,[20] which consists of a set of mass, charge, and momentum conservation equations. Ma et al. proposed a stationary, isothermal, 3-D model for the negative half-cell of a RFB, and showed that the electrolyte velocity has significant impact on the distributions of ion concentration, overpotential and transfer current density.[21] Qiu et al.[22] obtained detailed electrode's geometry using X-ray computed tomography. The image was used as input for simulation of the electrochemical processes in a RFB. They solved the coupled species and charge transport and predicted the RFB performance under various conditions. Watt-Smith et al.[23] employed a 2-D mathematical model to investigate charge-discharge performance and the effect of key process variables on cell efficiency. They also characterized several carbon felts for electrode activity.

Though several VFB models have been proposed, most of them consider simplified conditions, such as reduced dimension, half-cell operation, and isothermal condition. In addition, there are urgent needs for theoretical analysis and rigorous derivation to guide VFB fundamental study and technical development, including time constants, pumping power, local transport resistance, and dimensionless parameters. In this paper, we develop a full three-dimensional (3-D) RFB model by rigorously accounting for the conservation of mass, momentum, species, charges, and energy, in conjunction with the electrochemical reaction kinetics and species conservation in storage tanks. Discussions are presented for dilute solution approximation, negligible local mass transport resistance, H_2SO_4 dissociation, and pumping power for electrolyte flows. The 3-D dynamic system, coupling the RFB and electrolyte tanks, is numerically solved using the

[*]Electrochemical Society Active Member.
[z]E-mail: yunw@uci.edu

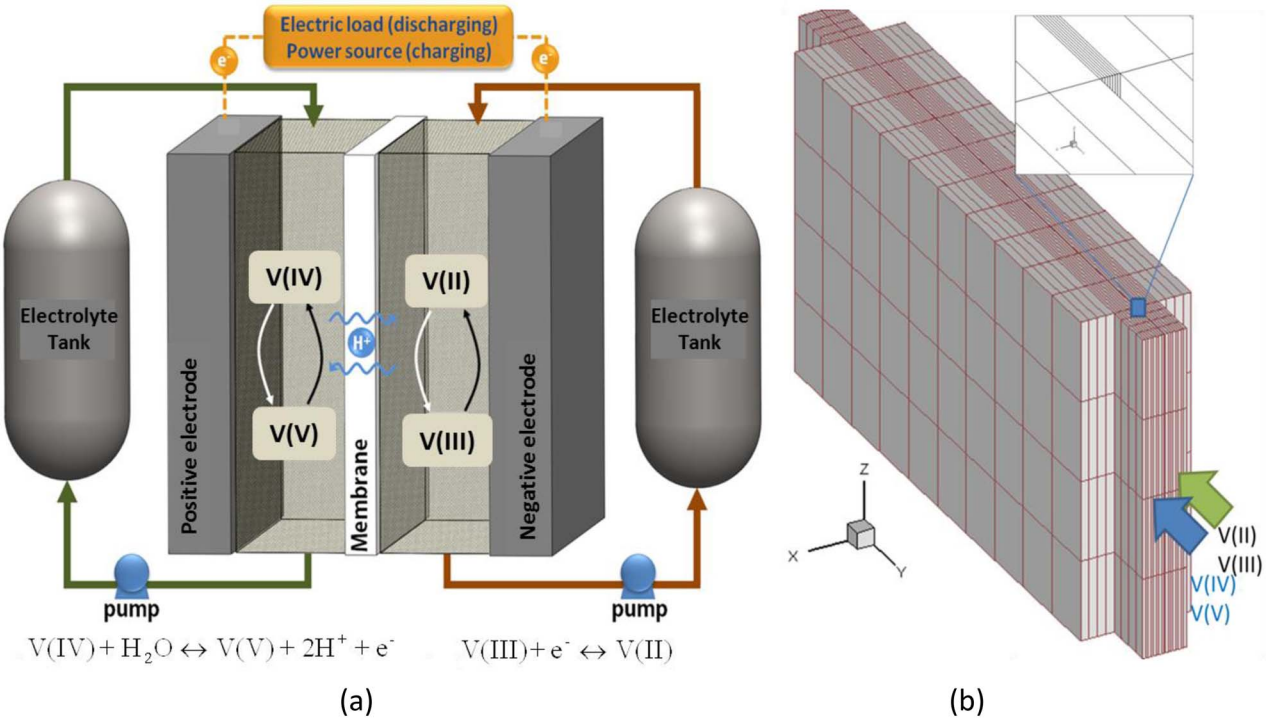

Figure 1. (a) Schematic of a flow battery (all vanadium redox flow battery as example); (b) Computational domain of the RFB in three-dimensional simulation.

finite volume method to predict the RFB dynamic performance and local vanadium species concentration and reaction rates. The model is validated against literature data for all the important operations, including charging, idling, and discharging. The time constants of mass and heat transfer and the Damköhler number are derived and discussed.

Mathematical Model

Flow battery model.— Fig. 1 schematically shows the geometry of a redox flow battery (RFB) and the constituent components to be modeled in this work, including current collectors, porous electrodes, membrane separator, and channels connected to reservoirs. The RFB model consists of a set of conservation equations for vanadium species (V(II), V(III), V(IV), and V(V)), H^+, charges, energy, mass, and momentum, in conjunction with the electrochemical reaction kinetics in both electrodes. The following assumptions are made: 1.) side reactions are ignored; 2.) porous electrodes are isotropic and homogeneous; 3.) the dilute-solution approximation holds true; 4.) the charge transfer kinetics is approximated by the Butler-Volmer equation; 5.) both H^+ and water can transport through the separator; 6.) local mass transport at the pore level is sufficiently fast. For 1.), side reactions such as hydrogen/oxygen evolution may take place, leading to bubble formation and two phase flow. Its effect on RFB performance, however, is usually small.[24,25] For 3.), liquid water is the dominant species in electrolytes. For a crude evaluation, the water concentration in pure liquid water is ~55,000 mol/m^3; while other ions are usually around 1,000 mol in electrolyte, thus the molar fraction of all the other species in the electrolyte is estimated to be:[26]

$$\frac{\sum_{j\neq H2O} C_j}{C_{H2O}} < 10\% \qquad [1]$$

The above ratio gives a measure of solution dilution, indicative of applicability of the dilute-solution approximation. For 5.), the membrane separator is selected to prevent the direct mixing of reactants. The cross-over must be kept low in order to avoid efficiency loss. For Nafion-based membranes (e.g. as those used in PEM fuel cells), water and protons are able to transport through the hydrophilic regions associated with the sulfonic acid groups.[27] With these assumptions, a 3-D RFB model of the electrochemical reactive flow system is developed and summarized below:

Electrochemical kinetics.—Battery electrodes are porous media with interconnected pore networks, enabling electrolyte flows. The electrochemical reactions take place at the interfaces of the electrolyte and solid structure, and are usually complex. The primary reaction (half-reaction) in the negative electrode is:

$$V(III) + e^- \underset{discharge-charge}{\longleftrightarrow} V(II) \quad (E^* = -0.255\,V \text{ vs. SHE}) \qquad [2]$$

In the positive electrode, the following electrochemical reaction occurs:

$$VO^{2+} + H_2O \underset{discharge-charge}{\longleftrightarrow} VO_2{}^+ + 2H^+ + e^- \quad (E^* = 1.004\,V \text{ vs. SHE}) \qquad [3]$$

where VO^{2+} and $VO_2{}^+$ represent V(IV) and V(V), respectively. The electrochemical reaction rate, j, see Table I, is evaluated by the Butler-Volmer equation, namely:

$$j = ai_0 \left\{ \exp\left(\frac{\alpha_a}{RT} \cdot F \cdot \eta\right) - \exp\left(-\frac{\alpha_c}{RT} \cdot F \cdot \eta\right) \right\} \qquad [4]$$

where α_a and α_c are anodic and cathodic charge transfer coefficients, respectively. The surface-to-volume ratio a describes the roughness of porous electrodes; while the exchange current density i_0 is a function of temperature, conventionally written in the Arrhenius form as follows:[28,29]

$$i_0 = i_{ref,0} \exp\left(-\frac{E_a}{R}\left[\frac{1}{T_{ref}} - \frac{1}{T}\right]\right) \qquad [5]$$

where E_a is the activation energy for the reaction and $i_{ref,0}$ is the values of i_0 at the reference temperature T_{ref}. Previous works[30–32] indicated that the kinetics of the V(IV)/V(V) reaction is much slower and more complex than that of V(II)/V(III) because vanadium ions at higher oxidation states tend to coordinate with oxygen ions. They also showed that the electrode reaction kinetics, especially in the positive

Table I. Source terms in the governing equations.[19–21,28]

Source term	Positive Electrode	Native Electrode	Others
$S_{V(II)}$	-	j_-/F	0
$S_{V(III)}$	-	$-j_-/F$	0
$S_{V(IV)}$	$-j_+/F$	-	0
$S_{V(V)}$	j_+/F	-	0
S_{H+}	$2j_+/F+S_d$	S_d	0
S_{HSO_4+}	$-S_d$	$-S_d$	0
$S_{\Phi^{(e)}}$	$2j_+$	0	0
$S_{\Phi^{(s)}}$	j_+	$-j_-$	0
S_u	$-\frac{\mu}{K}\vec{u}$	$-\frac{\mu}{K}\vec{u}$	0
S_T	$j_+T\Delta S + j\eta + \frac{i_e^2}{\kappa^{eff}} + \frac{i_s^2}{\sigma^{eff}}$	$j_-T\Delta S + j\eta + \frac{i_e^2}{\kappa^{eff}} + \frac{i_s^2}{\sigma^{eff}}$	$\frac{i_e^2}{\kappa^{eff}} + \frac{i_s^2}{\sigma^{eff}}$

side, are dramatically influenced by temperature. Thus, this study only accounts for the temperature dependence of the V(IV)/V(V) reaction kinetics, in which E_a was found to be 52.4 kJ mol^{-1} in the range of temperature 20–60°C for graphite electrodes.

The surface overpotential is defined as:

$$\eta = \Phi^{(s)} - \Phi^{(e)} - E_o \quad [6]$$

where E_o (V) is evaluated by the Nernst equation:

$$\text{Negative electrode}: E_o = E_o{}' + \frac{RT}{F}\ln\left(\frac{C_{V(III)}}{C_{V(II)}}\right)$$

$$\text{Positive electrode}: E_o = E_o{}' + \frac{RT}{F}\ln\left(\frac{C_{V(V)}}{C_{V(IV)}}\right) + \frac{2RT}{F}\ln C_{H+} \quad [7]$$

Under 25°C (or 298.15K), the equilibrium potentials are given by:[33]

$$\text{Negative electrode}: E_o = E^* + 0.05911\log\left(\frac{C_{V(III)}}{C_{V(II)}}\right)$$

$$\text{Positive electrode}: E_o = E^* + 0.05911\log\left(\frac{C_{V(V)}}{C_{V(IV)}}\right) - 0.1182pH \quad [8]$$

where the pH value is defined as:

$$\text{pH} = -\log(a_{H+}) \quad [9]$$

a_{H+} is the hydrogen ion activity. E_o is determined by the Gibbs free energy, and changes with temperature:[17]

Negative electrode :

$$E_o(T) = E_o(298.15K) + 1.5\times10^{-3}(T - 298.15K)$$

Positive electrode :

$$E_o(T) = E_o(298.15K) - 0.9\times10^{-3}(T - 298.15K) \quad [10]$$

It was indicated that the Butler-Volmer equation can be approximated by Tafel equation in the positive electrode, and by the linearized form in the negative electrode at voltage ranging from 0 to 2 V.[26]

At the pore level, the electrochemical reaction occurs at the surface of the solid matrix. For large pores, transport resistance between the bulk flow inside a pore and the reaction interface can be significant. To account for the resistance, the following formulas were used:[20]

$$j_1 = \varepsilon AFk_1\left(C^s_{V(III)}\right)^{\alpha_{-,1}}\left(C^s_{V(II)}\right)^{\alpha_{+,1}} \times\left\{\exp\left(\frac{\alpha_{+,1}F\eta_1}{RT}\right) - \exp\left(-\frac{\alpha_{-,1}F\eta_1}{RT}\right)\right\}$$

$$j_2 = \varepsilon AFk_2\left(C^s_{V(IV)}\right)^{\alpha_{-,2}}\left(C^s_{V(V)}\right)^{\alpha_{+,2}} \times\left\{\exp\left(\frac{\alpha_{+,2}F\eta_2}{RT}\right) - \exp\left(-\frac{\alpha_{-,2}F\eta_2}{RT}\right)\right\} \quad [11]$$

for the negative and positive electrodes, respectively, where A is the specific active surface area of the electrode (per unit volume); k is the standard rate constant for the reaction; α is the transfer coefficient; and η is the overpotential. The concentration differences between the bulk flow and reaction surface were derived as below:

$$C_{V(IV)} - C^s_{V(IV)} = \frac{\varepsilon k_1}{\gamma_{IV}}\left\{C^s_{V(IV)}\exp\left(\frac{F\left(\psi-\phi-E'_{0,2}\right)}{2RT}\right) - C^s_{V(V)}\exp\left(-\frac{F\left(\psi-\phi-E'_{0,2}\right)}{2RT}\right)\right\}$$

$$C_{V(V)} - C^s_{V(V)} = \frac{\varepsilon k_2}{\gamma_V}\left\{C^s_{V(IV)}\exp\left(\frac{F\left(\psi-\phi-E'_{0,1}\right)}{2RT}\right) - C^s_{V(V)}\exp\left(-\frac{F\left(\psi-\phi-E'_{0,1}\right)}{2RT}\right)\right\} \quad [12]$$

where $\gamma_{IV} = D_{IV}/d$ and$\gamma_V = D_V/d$, and δ is the average pore size in electrodes. The above formulas neglect pore-level convection effect, which is important for the pore size d $\sim 10^{-5}$ m, as indicated by the Peclet number ($Pe \sim \frac{convection}{diffusion}$):

$$Pe = \frac{vd}{D} \sim \frac{0.01m/s}{10^{-10}m^2/s}10^{-5}m = 10^3 \quad [13]$$

The local transfer coefficient k_m (or h_m) was used to evaluate the species transport between the bulk flow and reaction interface inside a pore.[19] In the positive electrode, the local flux at the reaction surface in charging is given by:

$$N^s_{IV} = k_m\left(C_{V(IV)} - C^s_{V(IV)}\right) = k_1(C_{V(IV)})^{\alpha_{1,c}}(C_{V(V)})^{\alpha_{1,a}} \times\left[\frac{C^s_{V(IV)}}{C_{V(IV)}}\exp\left(\frac{\alpha_{1,a}F\eta_1}{RT}\right) - \frac{C^s_{V(V)}}{C_{V(V)}}\exp\left(-\frac{\alpha_{1,c}F\eta_1}{RT}\right)\right]$$

$$N^s_V = k_m\left(C_{V(V)} - C^s_{V(V)}\right) = k_1\left(C_{V(IV)}\right)^{\alpha_{1,c}}\left(C_{V(V)}\right)^{\alpha_{1,a}} \times\left[\frac{C^s_{V(V)}}{C_{V(V)}}\exp\left(-\frac{\alpha_{1,c}F\eta_1}{RT}\right) - \frac{C^s_{V(IV)}}{C_{V(IV)}}\exp\left(\frac{\alpha_{1,a}F\eta_1}{RT}\right)\right] \quad [14]$$

which yields:

$$C^s_{V(IV)} = \frac{B_1C_{V(V)} + (1+B_1)C_{V(IV)}}{1+A_1+B_1} \text{ and}$$

$$C^s_{V(V)} = \frac{A_1C_{V(IV)} + (1+A_1)C_{V(V)}}{1+A_1+B_1} \quad [15]$$

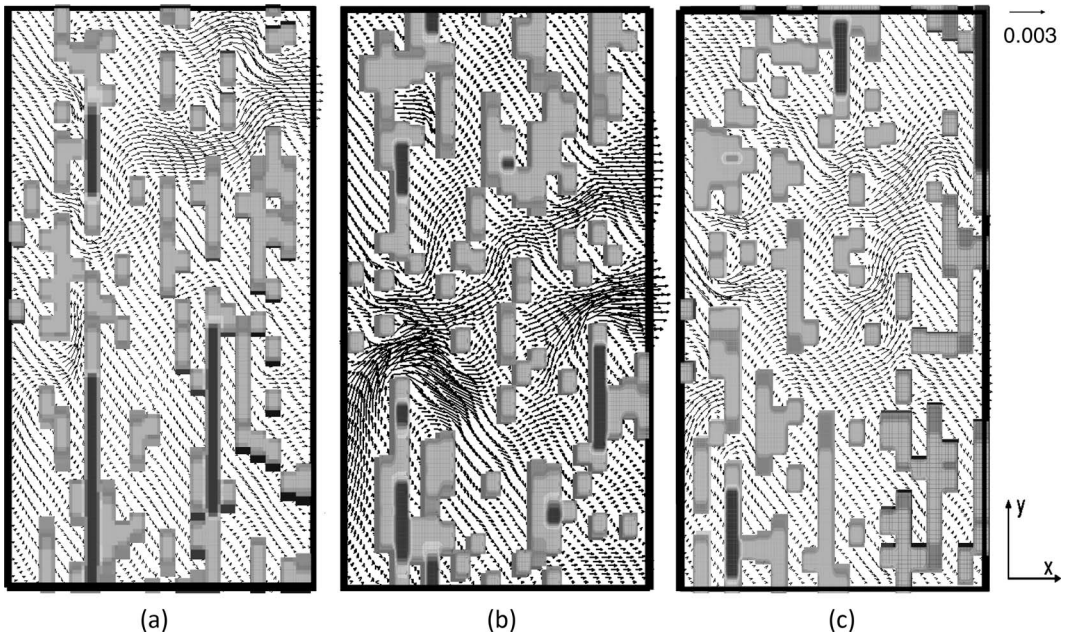

Figure 2. Micro flow fields in a carbon-fiber paper. (a-c) represents different cross sections. The gray region denotes the solid matrix with the light gray being the carbon fibers and the dark the binders.[35]

where A_1 and B_1 are expressed by:

$$A_1 = \frac{k_1}{k_m}(C_{V(IV)})^{\alpha_{1,c}-1}(C_{V(V)})^{\alpha_{1,a}} \exp\left(\frac{\alpha_{1,a} F\eta_1}{RT}\right) \text{ and}$$

$$B_1 = \frac{k_1}{k_m}(C_{V(IV)})^{\alpha_{1,c}}(C_{V(V)})^{\alpha_{1,a}-1} \exp\left(-\frac{\alpha_{1,c} F\eta_1}{RT}\right) \quad [16]$$

The mass transfer coefficient can be evaluated by[34]

$$k_m = 1.6 \times 10^{-4}\vec{v}^{0.4} \quad [17]$$

For the negative electrodes, similar expressions will be obtained:

$$C^s_{V(II)} = \frac{B_2 C_{V(III)} + (1 + B_2) C_{V(II)}}{1 + A_2 + B_2} \text{ and}$$

$$C^s_{V(III)} = \frac{A_2 C_{V(II)} + (1 + A_2) C_{V(III)}}{1 + A_2 + B_2} \quad [18]$$

where

$$A_2 = \frac{k_2}{k_m}(C_{V(II)})^{\alpha_{2,c}-1}(C_{V(III)})^{\alpha_{2,a}} \exp\left(\frac{\alpha_{2,a} F\eta_2}{RT}\right) \text{ and}$$

$$B_2 = \frac{k_2}{k_m}(C_{V(II)})^{\alpha_{2,c}}(C_{V(III)})^{\alpha_{2,a}-1} \exp\left(-\frac{\alpha_{2,c} F\eta_2}{RT}\right) \quad [19]$$

For the bulk flow velocity of 0.0025 m/s (i.e. v = 0.0025 m/s), the mass transfer coefficient k_m is 1.456×10^{-10} m/s using Eq. 17, yielding the Sherwood number (Sh = k_mL/D) around 1.5, for L = 10 μm and D = 10^{-10} m^2/s. This number is in the same order of magnitude of that in fully developed tube flows. In RFBs, the electrodes are usually unstructured porous medium, in which the solid matrix constantly alters flow direction at pore level. Fig. 2 displays micro flows within the pore structure of a carbon-fiber paper.[35] indicating undirected micro bulk flow toward, parallel to, or away from local solid surface, see Fig. 3. Similar flow fields were also predicted by Qiu et al.[22] As a result, undirected flows at pore level increase local mass transfer, yielding a more effective mass transfer than fully developed in tubes.

For analysis purpose, we assume diffusion is the only mechanism for species transport in bulk electrolyte in electrodes. The transport resistance yields a concentration difference between the bulk flow and reaction surface, evaluated by:

$$\Delta C = \frac{Id}{2aFD} \approx \frac{1000 \times 10^{-5}}{2 \times 10^3 \times 10^5 \times 10^{-10}} \sim 0.5\,\text{mol/m}^3 \quad [20]$$

where a represents the specific surface area ratio (usually ~100–1000 for porous electrodes), D is the diffusivity (~10^{-10} m^2/s), and d is the pore size (~10 μm). The resulting ΔC of about 0.5 mol/m^3 at 1000 A/m^2 is small, comparing with the bulk concentration of

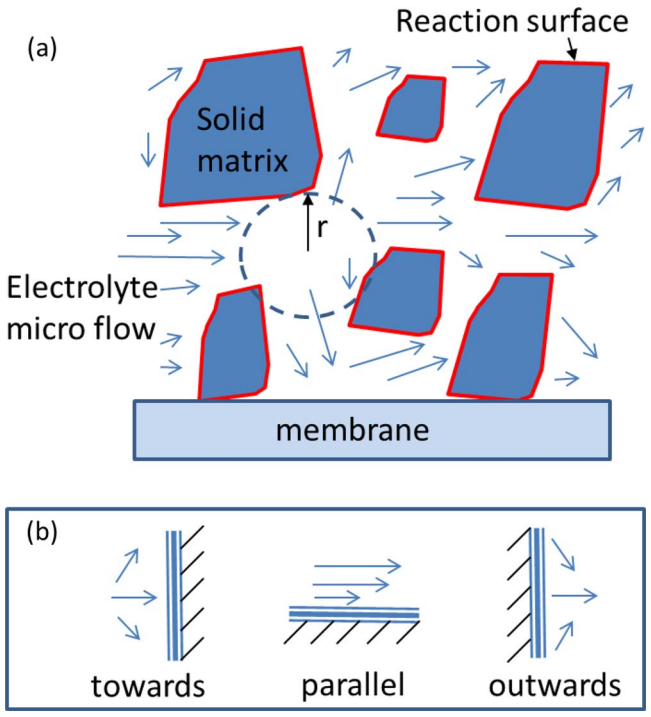

Figure 3. Schematic of (a): undirected micro flows of electrolyte at the pore level in electrodes; (b): flows towards, parallel to, and outwards the reaction surface.

reactants (~100–1000 mol/m^3). When taking into account convection effect (which is more effective than diffusion, as discussed), the variation will be much less than 0.5 mol/m^3. Thus, in this work we neglect the reactant concentration variation inside a pore or pore-level transport resistance. Furthermore, RFB operation is essentially transient, i.e. quantities constantly change with time. The time constant of species diffusion within a pore can be estimated by:

$$\tau_{D,i} = \frac{d^2}{D_i} \sim 1s \quad [21]$$

Comparing with common RFB operation which is in the timescale of minutes or hours, pore-level species transport is rapid.

The source term S_i, listed in Table I, represents the reaction rate of species i due to the electrochemical reactions or the dissociation of H_2SO_4. In vanadium RFBs, sulphuric acid is a popular electrolyte. In general, the dissociation of H_2SO_4 occurs in the following steps:

$$H_2SO_4 \rightarrow H^+ + HSO_4^-$$
$$HSO_4^- \rightarrow SO_4^{-2} + H^+ \quad [22]$$

Since the electrolytes contain less than the experimentally observed limit of H_2SO_4 (~40 mol/kg), it is safe to assume that the first step of dissociation ($H_2SO_4 \rightarrow H^+ + HSO_4^-$) is fully complete.[36,37] For the second step, the following formula was used for the dissociation rate:

$$S_d = k_d \left(\frac{C_{H+} - C_{HSO4-}}{C_{H+} + C_{HSO4-}} - \beta \right) \quad [23]$$

where k_d denotes the dissociation reaction coefficient, and β is the degree of dissociation of H_2SO_4. A constant β is assumed to equal to 0.4 in this study.[37]

Species conservation equation.—In electrolytes, the species of V(II), V(III), V(IV), and V(V) are the primary reactants or products during energy conversion. V(II) and V(III) are presented in the negative electrode for the redox electrochemical reaction, while V(IV) and V(V) are in the positive electrode. The conservation law of species can be formulated through the Nernst–Planck equation for the species flux:[38,39]

$$\frac{\partial \varepsilon C_i}{\partial t} + \nabla \cdot (\vec{u} C_i) = \nabla \cdot \left(D_i^{eff} \nabla C_i + \frac{z_i C_i D_i^{eff}}{RT} F \nabla \Phi^{(e)} \right) + S_i \quad [24]$$

where the effective diffusion coefficient D_i^{eff} is evaluated by the Bruggeman relation,

$$D_i^{eff} = \varepsilon^{\tau} D_i \quad [25]$$

In general, diffusion in liquids can be evaluated through the hydrodynamic model, which assumes the resistance of solute molecule movement arises from the viscous force, similar to particle movement in viscous fluids. In dilute liquid, the model yields the famous Stokes-Einstein equation:

$$D_i = \frac{k_B T}{6\pi r_i \mu} \quad [26]$$

where k_B is the Boltzmann's constant, r_i the molecular radius of the species i, and μ the electrolyte viscosity. In a solution that is not infinitely diluted, modification could be made by introducing the volume fraction of solute ε_i:[40]

$$D_i^* = D_i(1 + 1.45\varepsilon_i) \quad [27]$$

In porous electrodes, tortuosity τ measures the actual length of diffusive passage.[41] The MacMullin number (N_M), defined as the ratio of resistance of porous media saturated with an electrolyte to the bulk resistance of the same electrolyte,[42,43] is also used to evaluate the effectiveness of species diffusion:

$$N_M = \frac{D_i}{D_i^{eff}} = \frac{1}{f(\varepsilon, \tau)} \quad [28]$$

In Eq. 25, the MacMullin number is implicitly defined as $\varepsilon^{-\tau}$. Table III lists the expression of N_M for various porous media as a function of ε. In general, $f(\varepsilon, \tau)$ is determined by the pore-network structural characteristics such as pore shape and solid matrix arrangement.

In addition, diffusivity is a function of temperature, as shown by the Stokes-Einstein equation. Note that viscosity is affected by temperature. Ref. 29 adopted the Arrhenius equation for VO^{2+} diffusion:

$$D_i(T) = D_0 \exp\left(-\frac{E_d}{RT}\right) \quad [29]$$

where the activation energy Ed was found to be 10.52 kJ mol^{-1} based on their measurement.

In electrolytes, other species are present, including H^+, HSO^{4-}, and SO_4^{2-}. Their equations also follow the general conservation law.

In separators such as Nafion-series membranes, water and protons are able to transport. The conservation of water gives:[44]

$$\frac{\partial C_w}{\partial t} + \nabla \cdot (\vec{u}_l C_w) = \nabla \cdot \left(D_w^m \nabla C_w \right) \quad [30]$$

The conservation equation of protons follows the general ion transport in electrolytes. The separator is designed to prevent transport of other species such as vanadium ions to avoid reactant mixing. In reality, a small amount of cross-over occurs, leading to self-charging and capacity loss. Though diffusivity in the separator is generally very small, long-term operation may yield a significant amount of cross-over, reducing battery capability and efficiency. Table IV lists the typical diffusivity values of vanadium ions in the separator. The transport equation for vanadium ions in the separator is rewritten by:

$$\frac{\partial C_i}{\partial t} + \nabla \cdot (\vec{u}_l C_i) = \nabla \cdot \left(D_i^m \nabla C_i + \frac{z_i C_i D_i^m}{RT} F \nabla \Phi^{(e)} \right) \quad [31]$$

In separators such as Nafion membranes, fixed sulfonic acid charges are present in local, and remain immobile. Thus, their presence has no impact on the diffusion of mobile sulfonic acid ions, except that it influences the electric potential field. In the governing equation, the fixed sulfonic acid ions can be treated as a separate type of ions that is different with the mobile sulfonic acid ions. Assuming that protons are the only (or dominant) mobile ions, the proton concentration in separators can be evaluated through the electro-neutrality condition:

$$C_{H+} = -z_{HSO4} C^*_{HSO4} \quad [32]$$

where C^*_{HSO4} is the fixed-charge site (sulfonic acid) concentration in separators and z_{HSO4} is the fixed-site charge. In separators that are homogeneous, in absence of other ions proton diffusion is depressed due to fixed charges and local electro-neutrality. Thus, migration dominates proton transport. When considerable amounts of vanadium ions or other ions are present in separators, electro-neutrality gives:

$$C_{H+} = -z_{HSO4} C_{HSO4} - \sum_{\substack{rest \\ ions}} z_i C_i \quad [33]$$

Charge conservation equation (Phase potential equation).—The electric phase potential $\Phi^{(e)}$ influences ion transport. Its equation can be derived through charge conservation in electrolytes, and is given by:

$$0 = \nabla \cdot \left(\kappa^{eff} \nabla \Phi^{(e)} + F \sum_i z_i D_i^{eff} \nabla C_i \right) + S_{\Phi^{(e)}} \quad [34]$$

where $\Phi^{(e)}$ is the electric potential in the electrolyte and separators, and the effective ionic conductivity is given by:

$$\kappa^{eff} = \frac{F^2}{RT} \sum_i z_i^2 D_i^{eff} C_i \quad [35]$$

In the electrodes and current collectors, electric current flows are present, driven by the electronic phase potential $\Phi^{(s)}$, described by Ohm's law:

$$0 = \nabla \cdot (\sigma^{eff} \nabla \Phi^{(s)}) + S_{\Phi^{(s)}} \quad [36]$$

where the effective conductivity is evaluated by:

$$\sigma^{eff} = (1-\varepsilon)^{\tau_s}\,\sigma \quad [37]$$

In electrolytes, the total current flux is calculated by:

$$\vec{i}_e = -\kappa^{eff}\nabla\Phi^{(e)} - F\sum_i z_i D_i^{eff}\nabla C_i \quad [38]$$

In the electrodes and current collectors, the current flux is evaluated by:

$$\vec{i}_s = -\sigma^{eff}\nabla\Phi^{(s)} \quad [39]$$

The average current density is calculated through averaging current flux over a plane inside the separator or current collector:

$$I = \left|\iint_A \vec{i}_e\cdot d\vec{A}\right| = \left|\iint_A \vec{i}_s\cdot d\vec{A}\right| \quad [40]$$

In addition, there may exist electrical contact resistance between porous electrode and current collector. In the model, we develop a sub-model of the interfacial resistance and couple it with the electronic phase potential equations in the current collector and porous electrode. The value of the resistance was determined through fitting the experimental data, and is given in Table II.

Conservation of mass and momentum.—Liquid water in the electrolyte serves as solvent. We assume electrolyte flows are purely liquid water and incompressible, and write the continuity equation as below:

$$\nabla\cdot(\rho\vec{u}) = S_m \quad [41]$$

In operation, electrochemical reactions will alter the electrolyte composition and add/consume mass (S_m) to/from fluid flows. In PEM fuel cells, mass is added to the reactive flows via the catalyst layer,[45] which yields transverse flows at a magnitude of around 0.001 m/s. In RFBs, mass addition (S_m) is through electron transport via the electrode's solid matrix. Because electrolyte flows are liquid and hence much larger in density than those in PEM fuel cells, the influence of electrochemical activities on fluid flow is negligible. Thus, in this work, we assume $S_m = 0$. In the flow channels that connect to the RFB, the momentum conservation gives:

$$\nabla\cdot(\rho\vec{u}\vec{u}) = -\nabla P + \nabla\cdot\vec{\tau} \quad [42]$$

Table II. Geometrical and operating parameters.[19–22,26,56]

Quantity	Value
Electrode height/width/thickness	10/10/0.4 cm
Current collector/membrane thickness	6.3/0.2 mm
Electrode mean pore size, d	0.02 mm
Electrolyte volume in the tank, V	250 mL
Transfer coefficient for both electrodes, β	0.5
Faraday constant, F	96,487 C/mol
Electrical conductivity of electrode/current collector	500/1000 S/m
Hydraulic/Electro-kinetic permeability of separator	5×10^{-20} /1.13×10^{-19} m^2
Temperature, T_a/T_c	25°C
Negative/positive electrode volumetric inlet flow rate	1.0/1.0 mL/s
Pressure, P	3 atm
Current, I	10 A
Kinetic rate constant in negative electrode, k_1	1.75×10^{-7} m/s
Kinetic rate constant in positive electrode, k_2	3×10^{-9} m/s
Equilibrium potential in the negative/positive electrode	−0.255/1.004 V vs. NHE
Contact resistance between electrode and current collector	50 Ω m^2
Electrode volumetric porosity, ε	0.8

In the porous electrodes (carbon felts are the popular electrode material for vanadium RFBs), Darcy's law applies:

$$\vec{u} = -\frac{K}{\mu}\nabla P \quad [43]$$

where K is permeability, evaluated by the well-known Carman-Kozeny model:

$$K = \frac{\varepsilon^3}{180(1-\varepsilon)^2}d^2 \quad [44]$$

where d is the mean pore size and ε is volumetric porosity.

Pumping power is consumed to feed electrolyte flows into RFBs, which can be evaluated through the pressure drop and electrolyte volumetric flow rate. The pressure drop is determined by the flow rate and electrode permeability through Darcy's law. A parameter $\beta_{\text{Pumping power}}$ is defined below as the ratio of the pumping power to electric power produced by a RFB:[46]

$$\beta_{\text{Pumping power}} \approx \frac{\Theta_c\Delta P_c + \Theta_a\Delta P_a}{IV_{cell}A} = \frac{L\mu}{IV_{cell}AK}\left(\Theta_c u_c + \Theta_a u_a\right)$$
$$= \frac{L\mu A_{electrode}}{IV_{cell}AK}\left({u_c}^2 + {u_a}^2\right) \quad [45]$$

where Θ is the volumetric flow rate, L the electrode length, and u the electrolyte velocity. A and $A_{electrode}$ are the RFB's active and electrode's cross-section areas, respectively, and thus their ratio represents the geometrical feature of a RFB. Assuming that viscosity, electrolyte density, electrode permeability, cross-section area on both sides are equal, and the electrode and separator have the same in-plane length that is perpendicular to the channel flow and the electrodes are straight porous channels, i.e. $L = L_m$, the above formula can be rearranged to:

$$\beta_{\text{Pumping power}} \approx \frac{\mu\delta_{electrode}}{IV_{cell}K}\left({u_c}^2 + {u_a}^2\right) \xrightarrow{u_c=u_a=u} \frac{2\mu\delta_{electrode}u^2}{IV_{cell}K} \quad [46]$$

For the discharging in this study, I of 1,000 A/m^2, V_{cell} of ~0.9 V, $\delta_{electrode}$ of 0.4 cm, μ of 10^{-3} Pa s, and K of 5×10^{-11} m^2 yield $\beta_{\text{Pumping power}}$ of around 0.1%, indicative of a small amount of pumping power consumption. It is also consistent with the experimental work,[15] which indicates that the pumping power of electrolyte flows accounts for about 2–3% of energy generated.

The momentum equations of electrolyte flows for electrodes and inlet/outlet channels can be unified as below:

$$\frac{1}{\varepsilon^2}\nabla\cdot(\rho\vec{u}\vec{u}) = -\nabla P + \nabla\cdot\vec{\tau} + S_u \quad [47]$$

In separators, the liquid velocity $\vec{u}_l$ is given by the Schloegl's equation:

$$\vec{u}_l = -\frac{K_\Phi}{\mu_w}FC_{H+}\nabla\Phi^{(m)} - \frac{K_m}{\mu_w}\nabla P \quad [48]$$

where K_Φ is the electrokinetic permeability, K_m the hydraulic permeability, and C_{H+} the proton concentration.

Energy conservation equation.—In operation, waste heat is generated as a result of inefficiency in electric energy conversion. The waste heat is removed by electrolyte flows and the outer surfaces of the current collectors. Conservation of energy in RFBs gives:

$$\frac{\partial}{\partial t}\left(\overline{\rho C_p}T\right) + \nabla\cdot\left(\vec{u}\rho_l C_{P,l}T\right) = \bar{\lambda}\nabla^2 T + S_T \quad [49]$$

where ρ_l and $C_{P,l}$ are the of electrolyte density and specific heat capacity, respectively. The thermal conductivity $\bar{\lambda}$ and heat capacity $\overline{\rho C_p}$ are given by:

$$\bar{\lambda} = \begin{cases} \varepsilon\lambda_l + (1-\varepsilon)\lambda_s & Porous\ electrode \\ \lambda_m & Membrane \\ \lambda_c & Current\ collector \end{cases} \quad [50]$$

Table III. MacMullin number (N_M) of a system consisting of a dispersed non-conducting phase in a conductive medium.[43,55]

Label	Geometry	Arrangement	Size	Expression
I	Spheres	Random	Uniform	$N_M = \frac{(5-\varepsilon)(3+\varepsilon)}{8(1+\varepsilon)\varepsilon}$
II	Spheres	Cubic lattice	Uniform	$N_M = \frac{(3-\varepsilon)\left[\frac{4}{3}+0.409(1-\varepsilon)^{7/3}\right]-1.315(1-\varepsilon)^{10/3}}{2\varepsilon\left[\frac{4}{3}+0.409(1-\varepsilon)^{7/3}\right]-1.315(1-\varepsilon)^{10/3}}$
III	Spheres	Random and ordered	Range	$N_M = \varepsilon^{-1.5}$
IV	Cylinders	Parallel (square array)	Uniform	$N_M = \frac{2-\varepsilon-0.3058(1-\varepsilon)^4-1.334(1-\varepsilon)^8}{\varepsilon-0.3058(1-\varepsilon)^4-1.334(1-\varepsilon)^8}$
V	Fibrous material (Cylinders)	Random	-	$N_M = \frac{0.9126}{\varepsilon(\varepsilon-0.11)^{0.785}}$

and

$$\overline{\rho C_p} = \begin{cases} \varepsilon\rho_l C_{p,l} + \rho_s C_{p,s}(1-\varepsilon) & Porous\ electrode \\ \rho_m C_{p,m} & Membrane \\ \rho_c C_{p,c} & Current\ collector \end{cases} \quad [51]$$

The thermal properties of each phase j are listed in Table V. The source term S_T is given by:

$$S_T = jT\Delta S + j\eta + \frac{i_e^2}{\kappa^{eff}} + \frac{i_s^2}{\sigma^{eff}} \quad [52]$$

We neglect the viscous dissipation heating due to the low flow rate of electrolytes. The first term on the right represents the reversible reaction heating, derived through the thermodynamic relationship:

$$\Delta S = \int \frac{Q_{rev}}{T} \quad [53]$$

The second term on the right of Eq. 52 represents the irreversible reaction heating, arising from the presence of surface overpotential at the reaction interface. The third term is the Joule heating due to resistance to the ionic or electric current flows.

Table IV. Species condition and properties.[19,20,22]

Quantity	Value
V(II)/V(III) initial concentration	27/1053 mol/m^3
V(IV)/V(V) initial concentration	1053/27 mol/m^3
H^+/water initial concentration	1200/55, 500 mol/m^3
HSO_4^- initial concentration	1200 mol/m^3
SO_4^{2-} initial concentration in negative/positive electrode	1607/2174 mol/m^3
V(II)/V(III) diffusion coefficient in electrolyte	2.4×10^{-10} m^2/s
V(II)/V(III) diffusion coefficient in separator	$3.125/5.93 \times 10^{-12}$ m^2/s
V(IV)/V(V) diffusion coefficient in electrolyte	3.9×10^{-10} m^2/s
V(IV)/V(V) diffusion coefficient in separator	$5.0/1.17 \times 10^{-12}$ m^2/s
Water/proton diffusion coefficient in separator	$2.3/1.4 \times 10^{-9}$ m^2/s
SO_4^{2-}/HSO_4^- diffusion coefficient in separator	$2.2/1.23 \times 10^{-9}$ m^2/s
Fixed charge site (sulfonate acid) in separator C_{HSO4}	1200 mol/m^3
Fixed acid charge in separator z_{HSO4}	−1

Electrolyte tank model.— In operation, fresh fuel electrolytes are taken away from external tanks and fed into a RFB, while reacted electrolytes in the RFB is circulated back to the tanks and mix with the existing electrolyte. Assuming the tank is a system where species concentrations are uniform, i.e. the tank is a well-stirred system. Evolution of species concentration can be obtained through the species balance of the open system of the tank, given by:

$$\text{For products}: \quad \frac{dC_{i,\tan k}(t)}{dt} = \frac{|I|A}{FV}$$
$$\text{For reactants}: \quad \frac{dC_{i,\tan k}(t)}{dt} = -\frac{|I|A}{FV} \quad [54]$$

where A is the battery's active area, and V is the total volume of electrolyte in the tanks, recirculation pipes, and electrode pores. The initial condition is given by: $C_{i,\tan k} = C_{i,\tan k,0}$ at t = 0, where $C_{i,\tan k,0}$ is the initial concentration of species i prior to operation.

In this work, we use the V(III) concentration to define the state of charge (SOC):

$$SOC = 1 - \frac{\int_V C_{V(III)} dV}{\int_V C_{V(III),o} dV} \quad [55]$$

where the volumetric integral is over the electrode pore space, pipelines, and tanks; and $C_{V(III),o}$ represents the V(III) concentration at the full SOC state.

Boundary conditions.—The developed RFB model consists of a set of governing equations, along with their corresponding boundary conditions, described as below:

Inlet Boundary: Inlet velocity and species concentrations are set according to operating condition; and no-flux condition is applied for

Table V. Thermal properties.[17,28,57]

Quantity	Size
Electrolyte thermal conductivity λ_l	0.67 W m^{-1} K^{-1}
Electrode thermal conductivity λ_s	0.15 W m^{-1} K^{-1}
Membrane thermal conductivity λ_m	0.95 W m^{-1} K^{-1}
Current collector thermal conductivity λ_c	16 W m^{-1} K^{-1}
Liquid thermal capacitance (water) $\rho_l C_{P,l}$	4.187×10^6 J m^{-3} K^{-1}
Porous electrode thermal capacitance $\rho_s C_{P,s}$	3.33×10^5 J m^{-3} K^{-1}
Membrane thermal capacitance $\rho_m C_{P,m}$	1.65×10^6 J m^{-3} K^{-1}
Current collector thermal capacitance $\rho_c C_{P,c}$	4.03×10^6 J m^{-3} K^{-1}
Entropy change in the reaction Eq. 2), $-\Delta S$	−100 J mol^{-1} K^{-1}
Entropy change in the reaction Eq. 3, $-\Delta S$	−21.7 J mol^{-1} K^{-1}

the phase potentials:

$$u = u_{in},\ C_i = C_{i,\tan k}(t),\ T = T_{in},\ \text{and}\ \frac{\partial}{\partial n}\left(\begin{array}{c}\Phi^{(e)}\\ \Phi^{(s)}\end{array}\right)\Bigg|_{inlet} = 0 \quad [56]$$

Outlet Boundaries: Fully developed or no-flux conditions are applied

Walls: No-flux conditions are applied for all the walls except the outer surface of current collectors.

On the outer surface of the positive current collector:

$$-\sigma\frac{\partial}{\partial n}\Phi^{(s)}\Big|_{\substack{positive\\ current\\ collector}} = I \quad \text{and} \quad \mathrm{T} = \mathrm{T_p} \quad [57]$$

where I is the current density applied externally and n is the unit vector normal to the surface. A positive value of I means charging operation; whereas a negative refers to discharging operation.

On the outer surface of the negative current collector:

$$\Phi^{(s)} = 0 \,\text{and}\, \mathrm{T} = \mathrm{T_n} \quad [58]$$

Numerical Procedures

The governing equations along with their appropriate boundary conditions constitute a dynamic system, which is discretized using finite volume methods (FVM).[47] The "finite volume" refers to the small volume surrounding a node point in a computational mesh. In FVMs, a volumetric integral over a partial differential conservation equation that contains a divergence term (e.g. the convective or diffusive terms) is converted to surface integrals, based on the divergence theorem. The divergence term is then evaluated through the surface fluxes in each finite volume. Below gives a brief description of the FVM discretization.

It is convenient to unify all the governing equations, including the transient terms, in the following form:

$$\nabla\cdot\vec{\Gamma}(\Theta) = A_\Theta \quad [59]$$

where Θ stands for any dependent variable. Integrating the above equation throughout an arbitrary volume V bounded by a closed surface S yields:

$$\oint_S \vec{\Gamma}(\Theta)\cdot d\vec{S} = \int_V A_\Theta dv \quad [60]$$

where $\vec{S}$ is the surface vector. Taking V and S to be the volume V_p and discrete faces S_j of a computational cell, respectively, leads to:

$$\sum_j \int_{S_j} \vec{\Gamma}(\Theta)\cdot d\vec{S} = \int_{V_p} A_\Theta dv \quad [61]$$

The final discrete FVM equation can be expressed by:

$$B_p\Theta_p^n = \sum_m B_m\Theta_m^n + B\left(\Theta_p^0\right) \quad [62]$$

The above equation is then solved by the algebraic multi-grid (AMG) method. The solver is based on our in-house FORTRAN code developed for electrochemically reactive systems (originally for PEM fuel cells).[48] The solver specially includes an efficient numerical treatment for the two phase potential equations, which enables both current density and cell voltage virtual control over RFBs. The 3-D computational domain of the RFB is shown in Fig. 1 (b), and contains 3,400 computational elements. Grid dependence study was performed, showing further refining the mesh yields similar voltage prediction (difference <2%). The battery dimensions, operating parameters, and physical properties are listed in Table II. Adaptive time step is chosen: the present time step dt is inversely proportional to the voltage change during the previous time step, with the maximum time step < 0.1 s. In all the simulations to be presented in the next section, the equation residuals are set to be smaller than 10^{-7} in each time step. Each case, including the operations of charging, idling, and discharging, takes about 8 hours on a single node (AMD Opteron 2.20 GHz).

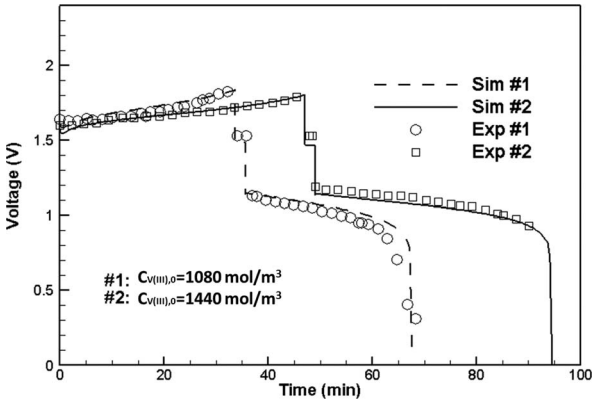

Figure 4. Comparison of predicted and experimental data for the RFB charging, idle, and discharging operations. Case #1 has the V(III) initial concentration of 1080 mol/m^3; Case #2 has 1440 mol/m^3. The experimental data were from Shah et al.[20]

Results and Discussion

Figure 4 compares the model prediction with experimental measurement[20] for charging, idling, and discharging under two operating conditions, and shows a good agreement between the two sets of data. The geometrical and experimental operating parameters were listed in Table II. Note that discrepancy exists particularly in the operation of discharging, which is likely due to the model assumptions such as ignorance of two-phase flow and side reactions. As the charging proceeds, voltage increases as a result of increasing "fuel" contents in the tanks. For the initial V(III) concentration of 1,080 mol/m^3, the charging was interrupted at 2,017 s and the battery was set at the idle state for two minutes. As no current is withdrawn during the two minutes of idling, the predicted voltage is actually the open circuit voltage (OCV), and remains almost constant. Following the idle operation, discharging applies under constant current. As current is withdrawn, considerable voltage loss arises due to irreversibility, leading to a sharp drop in voltage when applying discharging current. As discharging proceeds, more "fuel" is consumed, leading to a battery voltage drop and eventually a rapid drop when "fuels" are running out. Under the other condition (i.e. $C_{V(III),0}$ =1,140 mol/m^3), a similar trend was observed, except that charging or discharging takes longer time due to the more abundance of vanadium ions in the tank.

Figure 5 displays the flow fields in the RFB. The current collectors are impermeable, thus there are no fluids. Because they provide

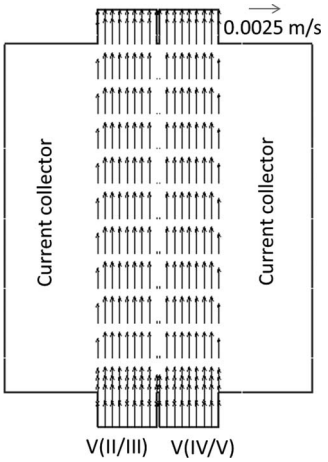

Figure 5. Flow field at the middle section of the RFB.

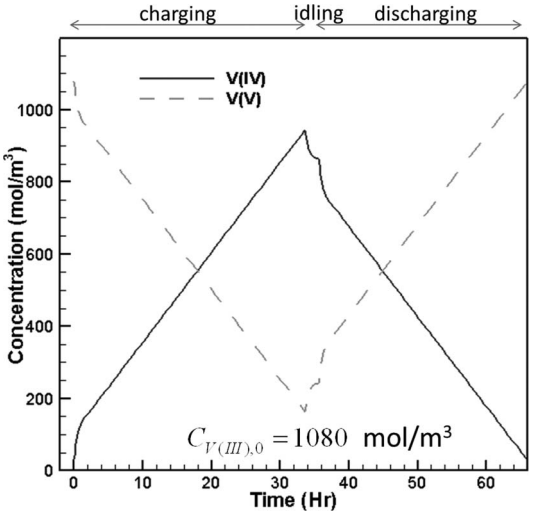

Figure 6. Evolutions of the average V(IV) and V(V) concentrations at the outlet for Case #1.

passages for cooling and electron transport for RFB operation, the current collectors are included in the computational domain. In the electrodes, electrolytes flow through the interconnected pore structure. Typical pore-level flows in a fiber-based medium are shown in Fig. 2.

In this study, we adopted the volume averaged velocity and Darcy's law, instead of detailed pore-level flow equations. In general, it is expensive to account for pore-level flows, which requires a full description of pore morphology. The volume averaging method is a popular approach for porous media, particularly when other phenomena are involved, e.g. multiphase flow, and chemical or electrochemical reactions. This figure shows that the average flows are almost uniformly distributed in the electrodes even near the separator. This is because the model assumes homogenous pore electrodes. In addition, in large RFBs, a set of parallel channels are usually adopted to distribute reactant fluid flows. In that case, phenomena such as channeling (flow bypassing) and flow mal-distribution need to be addressed, which can be added to the current model. In our previous work,[49,50] we modeled and discussed those phenomena for PEM fuel cells.

Figure 6 displays the predicted V(V) and V(IV) concentrations averaged at the respective outlets. In charging, the V(V) concentration decreases with time due to the electrochemical reaction consumption. In particular, a fast drop is present in the initial seconds, indicating that the reaction rapidly lowers the V(V) concentration inside the battery. After that, the change slows down and becomes almost linear with time till almost depletion. During the two minutes idling, the V(V) concentration recovers as a result of no reactions or V(V) consumption. The initial recovery at the outlet is rapid. In discharging operation, the V(V) concentration is increased by the electrochemical reaction production. A rapid increase is shown initially, followed by a linear increase. Furthermore, the rapid change, either drop or increase, occurs in a timescale of ~40 seconds, which is consistent with the

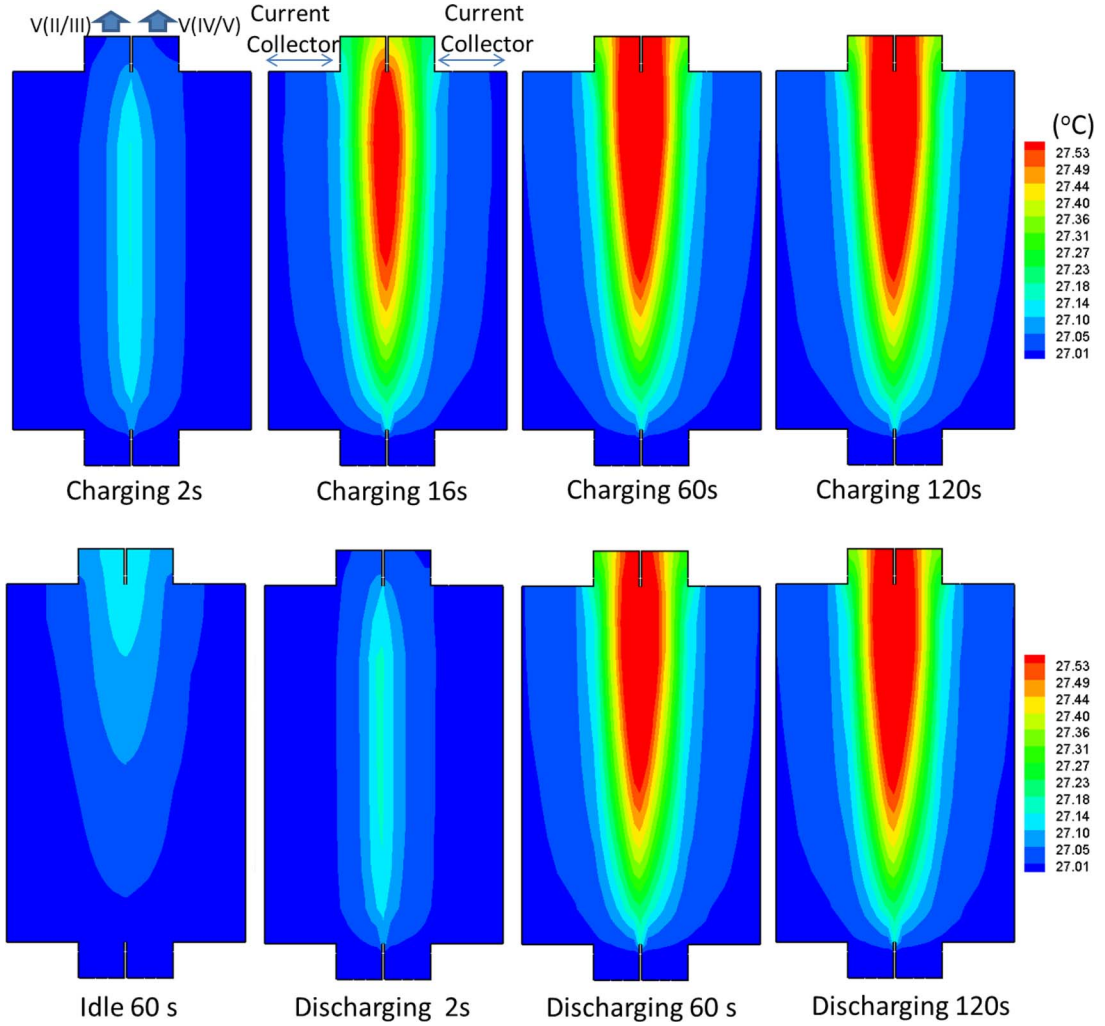

Figure 7. Temperature contours at the middle section of the RFB for Case #1.

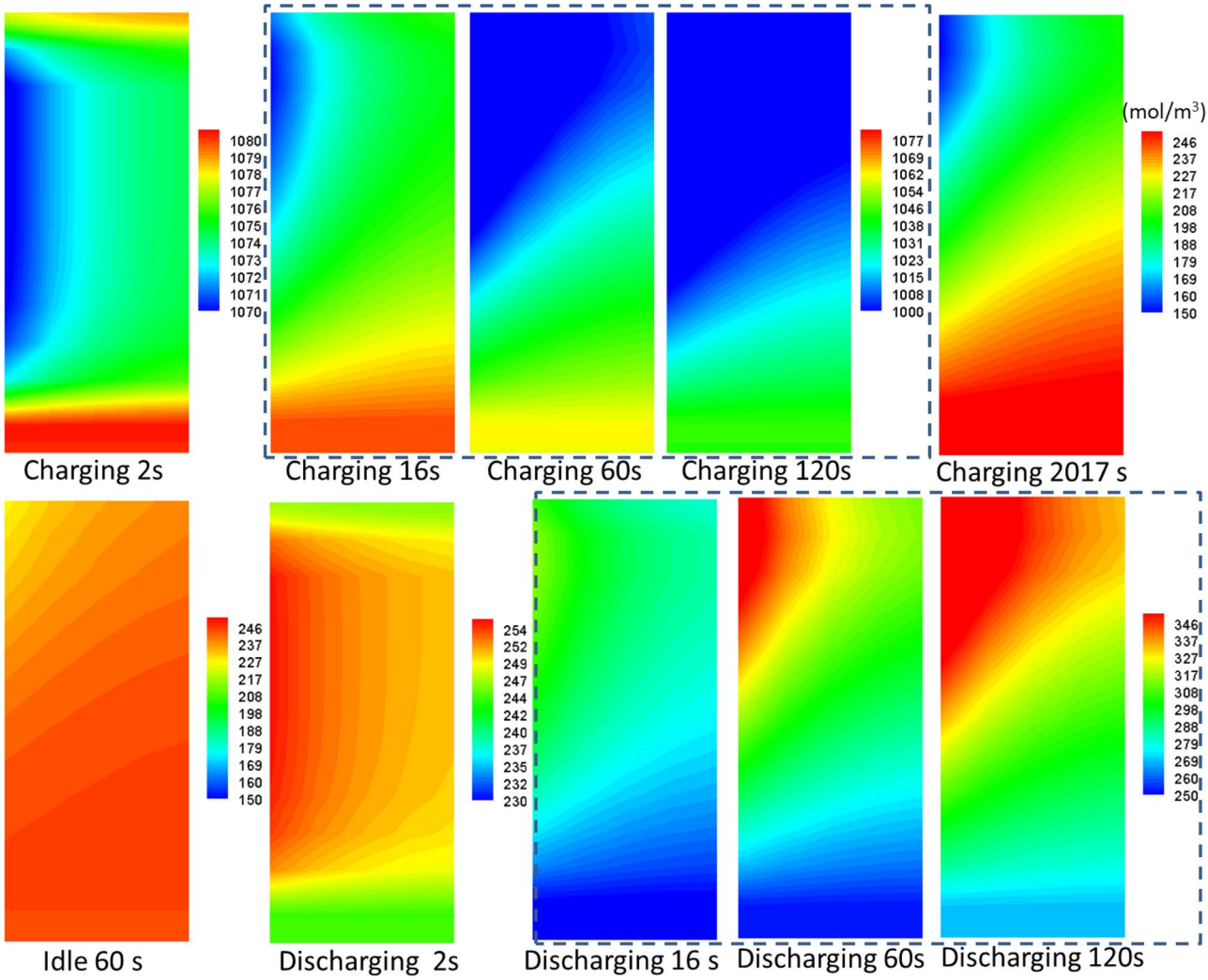

Figure 8. V(V) contours at the middle section of the RFB for Case #1.

time constant of species convection through the electrode, given by:

$$\tau_{u,i} = \frac{L}{U} \sim 40s \qquad [63]$$

Figure 7 presents the temperature contours in the battery's middle section during the three operations. It is seen that initially the RFB temperature is increased by addition of waste heat generated by the battery. Higher temperature is shown near the separator because partial cooling is provided by current collectors. At the 16th s into charging, temperature further increases with the peak shifting toward downstream due to heat convection by electrolyte flows. The RFB temperature keeps increasing till 60 s when it becomes stabilized, i.e. temperature changes little. The timescale of temperature increase is controlled by both heating and cooling. For the former, the time constant can be evaluated by:

$$\tau_{heating} = \frac{m\bar{C}_p \Delta T}{A\,|E - V_{RFB}|\,I} \qquad [64]$$

where $\bar{C}_p$ is the mean specific capability of a RFB and A represents the active reaction area. Given liquid water has a large specific capability and contributes to a major thermal mass of RFB, using the liquid water property and mass for $m\bar{C}_p$ will yield $\tau_{heating}$ around 10 seconds for ΔT ~0.5 K and $|E - V_{RFB}|$ ~0.3 V in this case. For the latter, electrolyte flows provide a major mechanism for cooling, with its time constant evaluated through the heat convection along the channel:

$$\tau_{u,cooling} = \frac{L}{U} \sim 40s \qquad [65]$$

The two time constants are in the same magnitude of that for temperature stabilization, observed in this figure. During the idling period (i.e. no reaction heating is produced), temperature steadily decreases as a result of the continuing cooling by electrolyte flows and current collector's surface. Due to the cooling by electrolyte flows, upstream temperature falls back to the room temperature first. As discharging starts, the reactions add waste heat to the battery, leading to temperature rise. Similarly, it takes about 60 s for temperature to be stabilized in discharging.

Figure 8 presents the V(V) contours in the middle section of the battery during the charging, idle, and discharging operations. Initially, low concentration appears in the portion of the electrode near the separator, due to the reaction consumption. At the initial 2 s in charging, it is clear that the V(V) content remains high near the outlet as the consumed upstream electrolyte has yet reached the outlet (the timescale for upstream reaching the outlet is ~40 s, as evaluated by Eq. 63). As more reactants are consumed downstream, the outlet concentration becomes lower. Different with temperature contours, the V(V) content keeps changing because the consumed V(V) is constantly added into the tank, which changes the tank's reactant content. During the idling, the tank's fresh electrolyte repels that inside the battery, leading to reactant recovery, as seen at the idle 60 s. In discharging, V(V)

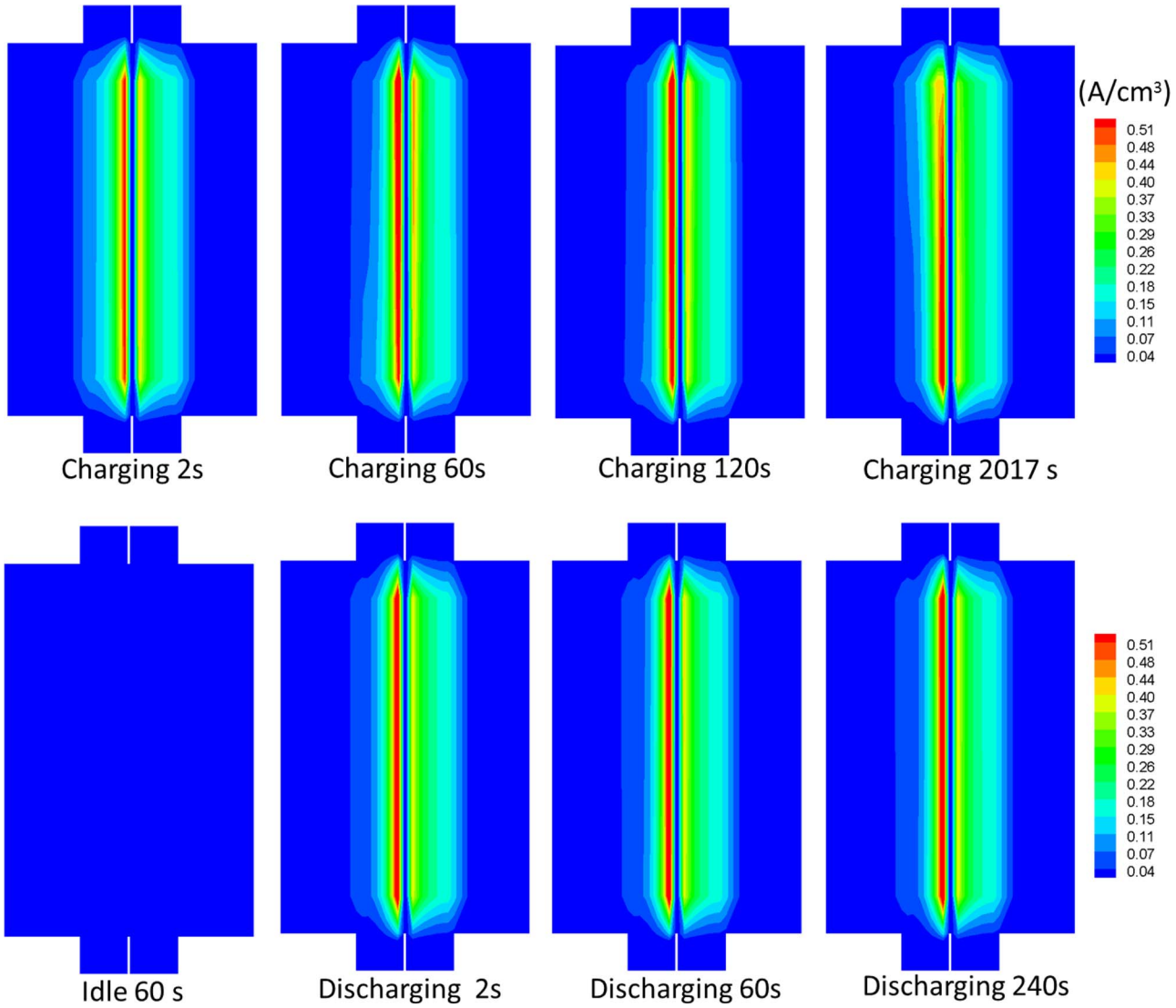

Figure 9. Charge transfer rate or transfer current density at the middle section of the RFB for Case #1.

becomes the reaction product; thus a higher concentration appears near the separator, where the local reaction rate is larger, as shown in Figure 9.

Figure 9 presents local charge transfer rate or transfer current density in both electrodes. This quantity represents the charge transferred rate locally, thus it indicates local electrochemical reaction activity. It appears in the source term of the phase potential equations, and links to the vanadium ions production/consumption rate through the Faraday's relation. This figure shows most charge production or consumption occurs in the portion of electrodes near the separator. Little difference is shown between the upstream and downstream in the initial period (~100 s). At the end of charging (i.e. t = 2,017 s), it clearly shows a decline in the charge transfer rate from the inlet area to outlet due to reactant depletion. In addition, reaction distributions change little in the initial stage (<120 s). Furthermore, the right electrode (V(IV)/V(V)) shows less variation in the charge transfer rate across the electrode, partly because of the higher diffusivities of V(IV) and V(V) than those of V(II) and V(III). Different with the pore-level transport resistance, the macroscopic diffusive resistance is significant in the transverse direction, as evidenced by the Damköhler (Da) number:

$$Da = \frac{I}{F}\frac{\delta}{C_V D^{eff}} = \frac{\text{Electrochemical reaction rate}}{\text{Mass diffusion rate}} \qquad [66]$$

Under common conditions, such as current density of 1,000 A/m^2, δ of 4 mm, C_V of 1,000 mol/m^3, and D^{eff} of 10^{-10} m^2/s, *Da* is around 400. It shows that diffusivity and electrochemical kinetics affect the value of Da. In the literature, a few measurements have been attempted to obtain the ion diffusivity, showing a range of values, e.g. for VO^{2+} or V(IV), the measured diffusivity is 1.86×10^{-10} m^2/s,[51] 0.889×10^{-10} m^2/s,[52] 4.4×10^{-9} m^2/s,[53] and 3.9×10^{-10} m^2/s.[54] In addition, the electrochemical kinetics is dependent on several factors, such as specific area (reaction surface roughness and pore structure) and catalyst materials. Liu et al. found that the exchange current density i_0 to be 2.4×10^{-3} A/cm^2, and the standard rate constant *k* is 1.2×10^{-5} cm/s at 20°C on graphite electrode.[29] During idling, the charge transfer rate becomes zero everywhere due to no reaction activity.

Conclusions

This work contributed to 1.) a three-dimensional model framework of RFBs; 2.) rigorous explanation of pore-level transport resistance, and pumping power; and 3.) timescale and dimensionless parameter analysis. The dynamic system consists of a set of conservation equations for mass, momentum, energy, and charges, in conjunction with the electrochemical reaction kinetics and fuel tank dynamics. Dilute solution assumption, pore-level mass transport resistance, pumping power for electrolyte flows and the time constants of a few

phenomenon were discussed. At pore level, the diffusion timescale and Peclet number are dependent on pore dimension, and were found to be around 1 seconds and 1,000, respectively, in the case of study. Analysis also indicated that electrolyte pumping power accounts for a very small portion of RFB power product (<0.1% in the case of study). The model was successfully implemented into three-dimensional simulation, and validated with experimental data for operations of charging, idling, and discharging. Local operating conditions, such as temperature contours, ion concentration distribution, flow field, and reaction rate, were investigated. It was observed that peak temperature appears near the separator initially, and then shifts to downstream for both charging and discharging operations. It takes about 60 s for temperature to be stabilized, which is consistent with the timescale analysis on heating (∼10 s) and convective cooling (∼40 s). The V(V) concentration at the outlet shows a rapid change in the initial seconds when switching operation. Most transfer current production occurs near the separator. The Damköhler (Da) number indicated that the macroscopic diffusive resistance is significant in the transverse direction, relative to the reaction kinetics. The transfer current changes little from the upstream to downstream during the initial periods of charging and discharging. The multi-dimensional tool is useful for virtual design and fundamental investigation of RFBs. Future work to further improve the RFB modeling include 1.) precisely incorporating multiphase flows, side reaction effects, heat-flow interaction in electrodes, and RFB degradation mechanisms; 2.) obtaining detailed experimental data for both material characterization such as electrochemical kinetics and comprehensive validation, e.g. local distributions; and 3.) developing advanced numerical schemes to efficiently simulate practical large-scale RFB operation.

Acknowledgment

We thank Dr. Xiao Guang Yang at Ford Motor Company and Prof. Partha Mukherjee at Texas A&M University for valuable discussion. Y. Wang also thanks NSF CBET for partial financial support (Award Number: 1336873). S.C. Cho thanks Sandia National Laboratories for past support.

List of Symbols

a	factor of effective catalyst area per unit volume
a_{H+}	hydrogen ion activity
C	molar concentration of species k, mol/m^3
D	species diffusivity, m^2/s
d	mean pore size, m
E_o	equilibrium potential, V
E_a	activation energy, kJ mol^{-1}
F	Faraday's constant, 96,487 C/mol
I	current density, A/cm^2
i	superficial current density, A/cm^2
j	charge transfer rate or transfer current density, A/cm^3
K	permeability, m^2
K_Φ	electrokinetic permeability, m^2
K_m	hydraulic permeability, m^2
k_d	dissociation reaction coefficient
k_m	mass transfer coefficient, m/s
M	molecular weight or molar mass, kg/mol
N_M	MacMullin number
R	universal gas constant, 8.134 J/mol K
r	mean pore radius, m
t	time, s
T	temperature, K
z_{HSO4}	fixed acid charge in separator

Greek

α	transfer coefficient
β	a constant; ratio; transfer coefficient
ρ	density, kg/m^3
ϕ	phase potential, V
σ	electric conductivity, S/m
κ	ionic conductivity, S/m
ε	volumetric porosity
η	surface overpotential, V
τ	tortuosity coefficient
δ	thickness, m
Θ	volumetric flow rate, m^3/s

Superscripts and Subscripts

D	diffusion
d	dissociation
e	electrolyte
eff	effective value
n	negative electrode
o	reference value; initial value
p	positive electrode
s	surface; solid

References

1. C. Ponce de Leon, A. Frías-Ferrer, J. González-García, D. A. Szánto, and F. C. Walsh, *Journal of Power Sources*, **160**(1), 716 (2006).
2. I. Tsuda, K. Nozaki, K. Sakuta, and K. Kurokawa, *Sol. Energy Mater. Sol. Cells*, **47**, 101 (1997).
3. M. Skyllas-Kazacos, M. H. Chakrabarti, S. A. Hajimolana, F. S. Mjalli, and M. Saleem, *J. Electrochem. Soc.*, **158**(8), R55 (2011).
4. A. M. Posner, *Fuel*, **34**, 330 (1955).
5. R. F. Savinell, Flow Batteries A Historical Perspective, *DOE Flow Battery Workshop*, (2012).
6. L. H. Thaller, *NASA* TM-X-71540 (1974).
7. L. H. Thaller, *NASA* TM-X-79143 (1979).
8. A. Z. Weber, M. M Mench, J. P. Meyers, P. N. Ross, J. T. Gostick, and Q. Liu, *J. Appl. Electrochem.*, **41**, 1137 (2011).
9. F. Walsh, *Pure Appl. Chem.*, **73**, 1819 (2001).
10. A. Parasuraman, T. M. Lim, C. Menictas, and M. Skyllas-Kazacos, *Electrochimca Acta*, **101**, 27 (2013).
11. P. K. Leung, X. Li, C. Ponce de Léon, L. Berlouis, C. T. J. Low, and F. C. Walsh, *RSC Advances*, **2**(27), 10125 (2012).
12. G. Kear, A. A. Shah, and F. C. Walsh, *International Journal of Energy*, **36**, 1105 (2011).
13. E. Sum and M. Skyllas-Kazacos, *J. Power Sources*, **15**, 179 (1985).
14. M. Rychcik and M. Skyllas-Kazacos, *J. Power Sources*, **22**, 59 (1988).
15. M. Skyllas-Kazacos, D. Kasherman, D. R. Hong, and M. Kazacos, *J. Power Sources*, **35**, 399 (1991).
16. M. Skyllas-Kazacos and C. Menictas, *Proceedings of 19th International Telecommunications Energy Conference-INTELEC 1997* (1997), 463.
17. H. Al-Fetlawi, A. A. Shah, and F. C. Walsh, *Electrochim Acta*, **55**, 78 (2009).
18. A. Shah, R. Tangirala, R. Singh, R. G. A. Wills, and F. C. Walsh, *J. Electrochem. Soc.*, **158**, A671 (2011).
19. D. You, H. Zhang, and J. Chen, *Electrochimica Acta*, **54**, 6827 (2009).
20. A. Shah, M. Watt-smith, and F. Walsh, *Electrochim Acta*, **53**, 8087 (2008).
21. X. Ma, H. Zhang, and F. Xing, *Electrochimica Acta*, **58**, 238 (2011).
22. G. Qiu, A. S. Joshi, C. R. Dennison, K. W. Knehr, E. C. Kumbur, and Y. Sun, *Electrochimica Acta*, **64**, 46 (2012).
23. Watt-Smith, H. Al-Fetlawi, P. Ridley, R. G. A. Wills, A. A. Shah, and F. C. Walsh, *Journal of Chemical Technology and Biotechnology*, **88**(1), 126 (2013).
24. A. A. Shah, H. Al-Fetlawi, and F. C. Walsh, *Electrochim. Acta*, **55**, 1125 (2010).
25. H. Al-Fetlawi, A. A. Shah, and F. C. Walsh, *Electrochim. Acta*, **55**, 3192 (2010).
26. M. Vynnycky, *Energy*, **36**, 2242 (2011).
27. K. A. Mauritz and R. B. Moore, *Chemical reviews*, **104**(10), 4535 (2004).
28. Y. Wang and C. Y. Wang, *J. Electrochem. Soc.*, **153** A1193 (2006).
29. H. J. Liu, Q. Xu, C. W. Yan, Y. Z. Cao, and Y. L. Qiao, *Int. J. Electrochem. Sci.*, **6**, 3483 (2011).
30. M. Gattrell, J. Qian, C. Stewart, P. Graham, and B. MacDougall, *Electrochim. Acta*, **51**, 395 (2005).
31. S. Zhong and M. Skyllas-Kazacos, *J. Power Sources*, **39**, 1 (1992).
32. Y. H. Wen, H. M. Zhang, P. Qian, H. P. Ma, B. L. Yi, and Y. S. Yang, *Chinese Journal of Chemistry*, **25**(3), 278 (2007).
33. M. Pourbaix, *Atlas of Electrochemical Equilibria in Aqueous Solutions*, second ed., NACE International, Houston, (1974) 236.
34. D. Schmal, J. Van Erkel, and P. J. Van Dnin, *J. Appl. Electrochem.*, **16**, 422 (1986).
35. Y. Wang, S. Cho, R. Thiedmann, V. Schmidt, W. Lehnert, and X. Feng, *International Journal of Heat and Mass Transfer*, **53**(5), 1128 (2010).
36. D. A. Knopf, B. P. Luo, U. K. Krieger, and T. Koop, *J. Phys. Chem.*, **107**, 4322 (2003).
37. K. W. Knehr, E. Agar, C. R. Dennison, A. R. Kalidindi, and E. C. Kumbur, *J. Electrochem. Soc.*, **159**(9), A1446 (2012).
38. W. M. Deen, *Analysis of Transport Phenomena*, Oxford University Press (1998).
39. J. Newman and K. E. Thomas-Alyea, *Electrochemical systems*, John Wiley & Sons (2012).

40. G. K. Batchelor, *Journal of Fluid Mechanics*, **74**, 1 (1976).
41. L. Shen and Z. Chen, *Chem. Eng. Sci.*, **62**, 3748 (2007).
42. T. Yeu, T. V. Nguyen, and R. E. White, *J. Electrochem. Soc.*, **135**(8), 1971 (1988).
43. M. J. Martínez, S. Shimpalee, and J. W. Van Zee, *J. Electrochem. Soc.*, **156**(1), B80 (2009).
44. T. E. Springer, T. A. Zawodzinski, and S. Gottesfeld, *J. Electrochem. Soc.*, **138**(8), 2334 (1991).
45. Y. Wang and C. Y. Wang, *J. Electrochem. Soc.*, **152**(2), A445 (2005).
46. Y. Wang, *J. Electrochem. Soc.*, **156**(10), B1124 (2009).
47. S. V. Patankar, *Numerical Heat Transfer and Fluid Flow*, Hemisphere Publishing Corp., New York (1980).
48. Y. Wang, *J. Power Sources*, **185**, 261 (2008).
49. Y. Wang, Ken S. Chen, J. Mishler, S. C. Cho, and X. C. Adroher, *Applied Energy*, **88**, 981 (2011).
50. Y. Wang, Suman Basu, and Chao-Yang Wang, *Journal of Power Sources*, **179**, 603 (2008).
51. S. Zhong and M. Skyllas-Kazacos, *J. Power Sources*, **39**, 1 (1992).
52. Y. H. Wen, H. M. Zhang, P. Qian, H. P. Ma, B. L. Yi, and Y. S. Yang, *Chin. J. Chem.*, **25**, 278 (2007).
53. X. G. Li, K. L. Huang, S. Q. Liu, and L. Q. Chen, *J. Cent. South Univ. T.*, **14**, 51 (2007).
54. T. Yamamura, N. Watanabe, T. Yano, and Y. Shiokawa, *J. Electrochem. Soc.*, **152**, A830 (2005).
55. Y. Wang, K. S. Chen, and S. C. Cho, *PEM Fuel Cells: Thermal and Water Management Fundamentals (Sustainable Energy)*, Momentum Press (2013).
56. A. J. Bard, R. Parsons, and J. Jordan, *Standard Potentials in Aqueous Solution*, Marcel Dekker, New York (1985).
57. M. Gattrell, J. Park, B. MacDougall, J. Apte, S. McCarthy, and C. Wu, *J. Electrochem. Soc.*, **151**, 123 (2004).